
This is an electronic reprint of the original article.
This reprint may differ from the original in pagination and typographic detail.

Järvinen, Riku; Alho, Markku; Kallio, Esa; Pulkkinen, Tuija

Ultra-low frequency waves in the ion foreshock of Mercury: A global hybrid modeling study

Published in:
Monthly Notices of the Royal Astronomical Society

DOI:
[10.1093/mnras/stz3257](https://doi.org/10.1093/mnras/stz3257)

Published: 01/01/2020

Document Version
Publisher's PDF, also known as Version of record

Please cite the original version:
Järvinen, R., Alho, M., Kallio, E., & Pulkkinen, T. (2020). Ultra-low frequency waves in the ion foreshock of Mercury: A global hybrid modeling study. *Monthly Notices of the Royal Astronomical Society*, 491(3), 4147-4161. <https://doi.org/10.1093/mnras/stz3257>

This material is protected by copyright and other intellectual property rights, and duplication or sale of all or part of any of the repository collections is not permitted, except that material may be duplicated by you for your research use or educational purposes in electronic or print form. You must obtain permission for any other use. Electronic or print copies may not be offered, whether for sale or otherwise to anyone who is not an authorised user.

Ultra-low-frequency waves in the ion foreshock of Mercury: a global hybrid modelling study

R. Jarvinen ^{1,2}★, M. Alho,¹ E. Kallio¹ and T. I. Pulkkinen ^{1,3}

¹Department of Electronics and Nanoengineering, School of Electrical Engineering, Aalto University, Maarintie 8, FI-02150 Espoo, Finland

²Finnish Meteorological Institute, Erik Palmenin aukio 1, FI-00560 Helsinki, Finland

³Department of Climate and Space Sciences and Engineering, University of Michigan, 2455 Hayward St., Ann Arbor, MI 48109-2143, USA

Accepted 2019 November 18. in original form 2019 October 23

ABSTRACT

We study the solar wind interaction with Mercury using a global three-dimensional hybrid model. In the analysed simulation run, we find a well-developed, dynamic Hermean ion foreshock ahead of the quasi-parallel bow shock under upstream solar wind and interplanetary magnetic field (IMF) conditions corresponding to the orbital perihelion of the planet. A portion of the incident solar wind ion flux is scattered back upstream near the quasi-parallel bow shock including both major solar wind ion species, protons and alphas. The scattered particles form the Hermean suprathermal foreshock ion population. A significant part of the suprathermal population is backstreaming with a velocity component towards the Sun in the near-foreshock at the planetocentric distance of few planetary radii in the plane of the IMF. The ion foreshock is associated with large-scale, oblique fast magnetosonic waves in the ultra-low-frequency (ULF) range convecting downstream with the solar wind. The ULF wave period is about 5 s in the analysed upstream condition case at Mercury, which corresponds to the 30-s foreshock waves at Earth when scaled by the IMF magnitude.

Key words: magnetic fields – plasmas – waves – solar wind – planet–star interactions.

1 INTRODUCTION

Mercury is the closest planet to the Sun. It is the smallest planet and has the highest uncompressed mass density of the Solar system planets. This indicates that Mercury contains a lot of heavy elements such as iron. The iron-rich core of the planet is estimated to fill more than half of its volume (Hauck et al. 2013). Mercury has no atmosphere, but processes near the surface release planetary material in space forming a tenuous exosphere (Killen et al. 2007). Mercury has a global intrinsic magnetic field. A comparison using a dipolar approximation of planetary magnetic fields shows that the strength of the Hermean surface magnetic field equals to Earth's magnetic field at the planetocentric distance of about 5.5 Earth radii (Finlay et al. 2010; Anderson et al. 2011; Johnson et al. 2012).

Mercury has an eccentric orbit with a perihelion at a distance of 0.31 au and an aphelion at a distance of 0.47 au from the Sun. This means that Mercury receives from more than twice to almost 30 times the solar irradiance compared to the orbits of the other three terrestrial planets of the Solar system. The same inverse distance squared scaling applies to the solar wind density, and also the temperature of the solar wind ions decreases with increasing distance to the Sun (Gazis & Lazarus 1982). The Sun's magnetic

field spreads in the heliosphere, frozen-in to the solar wind flow, and forms the Parker spiral of the interplanetary magnetic field (IMF) (Parker 1958). The Parker spiral angle is the angle between the IMF and the solar wind flow. It is 17° in the case of the away-from-the-Sun sector of the IMF at Mercury's orbital perihelion (Slavin & Holzer 1981). This means that the IMF is the most flow-aligned (or anti-aligned in the case of the towards-the-Sun sector), and has the strongest magnitude at Mercury of all the Solar system planets.

Mercury is a unique object from the point of view of solar wind–magnetosphere interactions. It provides an opportunity to study a considerably smaller magnetosphere under more extreme solar wind and IMF conditions compared to other magnetized planets within the reach of *in situ* exploration missions. The interaction of the magnetized solar wind with the magnetic field of Mercury results in a wide range of space weather phenomena (see, for example, Slavin et al. 2014, and references therein). Like at other globally magnetized planets, the magnetosphere of Mercury is separated from the solar wind flow by the magnetopause and the turbulent magnetosheath region forms downstream of the bow shock. However, unlike at other magnetospheres, the moderate strength of the Hermean global magnetic field means that the planet fills a considerable portion of its solar wind interaction region. Furthermore, Mercury has no ionosphere, which could, for example, provide closure for magnetospheric electric currents near the planet. For these reasons, many of the Hermean space weather processes

* E-mail: riku.jarvinen@aalto.fi

occur on significantly faster temporal scales compared to Earth (e.g. Imber & Slavin 2017).

Interesting questions related to the ‘pocket-size’ magnetosphere of Mercury include the properties of the bow shock and the foreshock, the outermost parts of a planetary solar wind interaction region. The foreshock is an upstream region magnetically connected to the bow shock, and includes backstreaming solar wind particles reflected at the bow shock or magnetosheath particles transported upstream through the bow shock (Eastwood et al. 2005). Electron reflections can occur almost everywhere where an upstream region connects to a bow shock; this region has been termed the electron foreshock. In the case of the ion foreshock, the reflections occur in the quasi-parallel region of the bow shock where the angle between the shock normal and the upstream magnetic field (θ_{Bn}) is less than $\sim 45^\circ$. Another requirement for ion reflection is that the magnetosonic Mach number of a bow shock is above a critical value, i.e. that the shock is supercritical. The supercriticality is associated with shock dissipation processes causing a portion of incident ion flux reflect back in an upstream region. This critical Mach number is larger than 1 and at maximum 2.76 for a resistive fast collisionless shock, and up to about 3.4 when thermal conduction is taken into account, in the magnetohydrodynamic (MHD) approximation with a dependence on plasma beta and θ_{Bn} (Marshall 1955; Edmiston & Kennel 1984; Kennel 1987; Treumann 2009; Parks et al. 2017). Below the critical Mach number the shock can dissipate incident energy without ion reflections.

It is interesting to note that the upstream magnetosonic Mach number varies in the range of 3.2–4.2 and plasma beta in the range of 0.5–0.9 from perihelion to aphelion under nominal solar wind conditions at Mercury (see tables 1 and 2 in Slavin & Holzer 1981). The variations are due to the dependence of the Alfvén and sound speed and beta on the IMF strength and the density and temperature of the solar wind particle species. The range for beta means that the corresponding critical Mach number is typically at maximum ~ 2 depending on the polytropic index of the solar wind plasma (Edmiston & Kennel 1984). That is, while the Hermean bow shock is typically supercritical, especially at the perihelion it has a Mach number on average smaller compared to other Solar system planets due to the solar wind temperature, density, and IMF strength. Statistical analysis of the solar wind and IMF conditions at Mercury show occurrences of the estimated Alfvén Mach number as low as 2 (Winslow et al. 2013). To our knowledge, there is no detailed analysis of ion observations in the foreshock of Mercury, and it is not well established how extended the Hermean ion foreshock is.

Magnetic wave activity in the foreshock of Mercury has been measured by both spacecraft missions that have observed the planet *in situ*: Mariner 10 (flybys) and the MErcury Surface, Space ENvironment, GEochemistry, and Ranging (MESSENGER) orbiter. Two main classes of magnetic field waves in the ultra-low-frequency (ULF) range (~ 1 mHz–10 Hz) have been reported upstream of the Hermean bow shock (Fairfield & Behannon 1976; Uritsky et al. 2011; Le et al. 2013): high-frequency whistler waves in the range of about 0.5–4 Hz (0.25–2 s) and low-frequency fast magnetosonic waves in the range of about 0.1–0.5 Hz (2–10 s). Note that we refer to wave frequencies with the corresponding wave periods in parenthesis and vice versa in this study. The whistlers occur in long-lasting wave trains and have dominated the upstream wave measurements by MESSENGER during the first 2 months of the mission when Mercury moved from orbital perihelion to aphelion (Le et al. 2013). Observations of the fast magnetosonic waves were associated with the quasi-parallel bow

shock. At Earth, these correspond to the 30-s foreshock waves excited by the suprathermal foreshock ion populations (Hoppe & Russell 1982; Orłowski, Crawford & Russell 1990; Gary 1991). The observed amplitude of the fast magnetosonic foreshock waves is only $\delta B/B \sim 10$ per cent at Mercury (Le et al. 2013), whereas at Earth they occur at small amplitudes as well as amplitudes similar to the IMF strength ($\delta B/B \sim 100$ per cent) (Omidi, Blanco-Cano & Russell 2005). This difference in the amplitude between the two planets can be attributed to a smaller bow shock and foreshock size, and, thus, a shorter growth time of the ULF waves convecting with the solar wind in the foreshock, and a weaker backstreaming ion flux or even the lack of the backstreaming ions at Mercury compared to Earth (Le et al. 2013).

Mercury’s solar wind interaction has been studied in several three-dimensional hybrid simulation works, where the ions of solar wind and planetary origin are treated kinetically as particles and electrons are a fluid. Studied topics in hybrid models include, for example, the structure and dynamics of the Hermean magnetosphere (Kallio & Janhunen 2004; Trávníček, Hellinger & Schriver 2007; Richer et al. 2012; Fatemi et al. 2018) and its electric currents and boundaries (Omidi et al. 2006; Exner et al. 2018), the solar wind precipitation in the planet’s surface, and the formation of the exosphere (Pfleger et al. 2015). In some models, the ion foreshock forms ahead of Mercury’s quasi-parallel bow shock, most likely depending on model resolution and the used upstream conditions (Omidi et al. 2006; Trávníček et al. 2007; Fatemi et al. 2018). While plasma waves have been studied in the Hermean magnetosphere and magnetosheath in some three-dimensional hybrid modelling works, analysis of waves in the foreshock of Mercury in these models has not been published to our knowledge.

Here, we present a study of the solar wind interaction with Mercury using a global three-dimensional hybrid simulation approach. In our simulation case, we use nominal solar wind and IMF conditions at the orbital perihelion of Mercury and analyse large-scale ULF plasma waves in the ion foreshock. The study is organized as follows. First, we describe the model and the simulation run. Then, we present and discuss the results, and finally in Section 5 the findings of our research are summarized.

2 MODEL

We use a three-dimensional global quasi-neutral hybrid simulation model to analyse the Hermean solar wind interaction. In the model, ions are treated as kinetic particles and their dynamics are self-consistently coupled with the temporal evolution of the magnetic field via the ion electric current density and the ion electric charge density. Electrons are a charge-neutralizing fluid. The Mercury model is implemented on a highly parallel C++ hybrid simulation platform for planetary plasma interactions named RHybrid (Jarvinen et al. 2018). Here, we describe the most important details of the numerical algorithm for the current analysis. See Kallio & Janhunen (2003, 2004) for further details of the algorithm.

The simulation space near a planet is divided into cubic, constant-sized cells with the side length Δx forming the Cartesian simulation grid. Ions are treated as macroscopic particle clouds (macroparticles or macroions) moving under the Lorentz force within the grid cells. Each macroparticle represents a number of real physical particles with the same velocity, particle charge, and particle mass. The size and shape of a particle cloud are the same as those of a grid cell. A statistical weighting factor is used in the tri-linear cloud-in-cell (CIC) accumulation of particle moments in the grid. The electrons are modelled as a massless and pressureless fluid. The state of

the simulation is advanced in time over the time-step Δt using a leapfrog algorithm as follows.

Macroparticles are accelerated by the Lorentz force and then moved by Newton's second law

$$\frac{d\mathbf{v}_i}{dt} = \frac{q_i}{m_i} (\mathbf{E}_L + \mathbf{v}_i \times \mathbf{B}) \quad (1)$$

$$\frac{d\mathbf{x}_i}{dt} = \mathbf{v}_i, \quad (2)$$

where \mathbf{v}_i and \mathbf{x}_i are the velocity and position of a macroparticle, q_i , m_i are the electric charge and mass of the particle species that a macroparticle represents, \mathbf{B} is the magnetic field, $\mathbf{E}_L = -\mathbf{U}_E \times \mathbf{B}$ is the electric field, and \mathbf{U}_E is the electron velocity. In the moving procedure, the ion electric charge density ($\rho_{q, \text{ion}}$) and the ion electric current density (\mathbf{J}_{ion}) are accumulated in the grid at a half time-step between the present and next simulation temporal states

$$\rho_{q, \text{ion}} = \sum_s q_s n_s \quad (3)$$

$$\mathbf{J}_{\text{ion}} = \sum_s q_s n_s \mathbf{U}_s, \quad (4)$$

where the summation extends over all ion species s in a cell, n_s is the number density of the ion species s in a cell, and \mathbf{U}_s is the bulk velocity of the ion species s in a cell. The density of the species s is computed as $n_s = \sum_i (w_i \Delta V_i) / \Delta V$, where the summation extends over all macroions of the species s overlapping with the cell, w_i is the number of real particles a macroion represents (the statistical weight of a macroion), ΔV_i is the portion of the volume that a macroion overlaps with the cell and $\Delta V = \Delta x^3$ is the cell volume. The bulk velocity of the species s is determined similarly as $\mathbf{U}_s = \sum_i (\mathbf{v}_i w_i \Delta V_i) / \sum_i (w_i \Delta V_i)$.

The total electric current density is derived from the magnetic field by Ampère's law

$$\mathbf{J} = \nabla \times \mathbf{B} / \mu_0 \quad (5)$$

and the electron charge density in each cell is determined by the quasi-neutrality condition

$$q_E n_E = -\rho_{q, \text{ion}} \quad (6)$$

where q_E is the electron electric charge and n_E is the electron number density. Note that the electron charge density is a CIC accumulated variable in the simulation run analysed here, whereas the densities of individual ions species shown in the figures are determined using a nearest grid point (NGP) interpolation. That is, the accumulated electron density has less macroparticle noise than the ion densities. The velocity of the electron fluid is calculated from the total electric current density (equation 5), the ion electric current density (equation 4), and the electron charge density (equation 6).

$$\mathbf{U}_E = (\mathbf{J} - \sum_s q_s n_s \mathbf{U}_s) / (q_E n_E) \quad (7)$$

Finally, the magnetic field is propagated by Faraday's law

$$\partial \mathbf{B} / \partial t = -\nabla \times \mathbf{E}_F \quad (8)$$

where $\mathbf{E}_F = -\mathbf{U}_E \times \mathbf{B} + \eta_a \mathbf{J}$.

Note that the electric field in the Lorentz force (equation 1) includes the ion convection term ($-\mathbf{U} \times \mathbf{B}$, where \mathbf{U} is the plasma bulk velocity) and the Hall term ($\mathbf{J} \times \mathbf{B} / \rho_{q, \text{ion}}$). In addition to these two terms, the electric field in Faraday's law (equation 8) includes the resistive term $\eta_a \mathbf{J}$ (Ledvina, Ma & Kallio 2008). The resistivity η_a is used to add explicit diffusion in the propagation of the magnetic field, and it can be a fully three-dimensional function. The value of

η_a above the superconducting core of Mercury (see Table 1) was set such that the magnetic diffusion time becomes $\tau_d = \Delta t / 7 \times 10^{-3} \approx 140 \Delta t$. This was moderate enough to allow some diffusion to stabilize the numerical integration while in the same time small enough to keep the solution from becoming smoothed out. η_a has the same order of magnitude as in our earlier work (Jarvinen et al. 2018). The magnetic field is stored on grid cell faces between time-steps, and Faraday's law is integrated as a loop over cell-face edges. This staggered set-up guarantees that the initially divergence-free magnetic field will stay divergence-free in the integration.

The following constraints were applied in the solving of the equations. In order to control the rate of the magnetic field growth, a roof value was used for the magnitude of the electric field in equation (8). The electric field magnitude roof works so that the vector \mathbf{E}_F is replaced by the vector $\mathbf{E}_F E_{\text{max}} / |\mathbf{E}_F|$ if $|\mathbf{E}_F| > E_{\text{max}}$. The roof value was set at about 16 times the magnitude of the undisturbed upstream convection electric field: $E_{\text{max}} = 90.6 \text{ mV/m} \approx 15.7 |\mathbf{V}_{\text{sw}} \times \mathbf{B}_{\text{sw}}|$. This gives the maximum growth rate of the magnetic field of $\Delta B / \Delta t = E_{\text{max}} / \Delta x \approx 557 \text{ nT/s}$. The same method was used to implement roof values for the macroion velocity and the velocity of the electron fluid with the roof speeds set at 4000 km s^{-1} to prevent violation of the Courant–Friedrichs–Lewy (CFL) condition. Further, also the whistler wave propagation was controlled by limiting the total electric current density in equation (5) if the whistler wave speed exceeded 4000 km s^{-1} (see equation 3.17 in Alho 2016). A floor value was set to limit the ion charge density at $\rho_{q, \text{ion}} \geq 0.315 \text{ e/cm}^3$, which at the minimum equals to 0.4 per cent of the undisturbed upstream solar wind ion charge density.

Note the following differences in the current parallelized simulation code (Jarvinen et al. 2018) compared to our earlier work (Kallio & Janhunen 2003): the electric current density is evaluated at the edges of the grid cell faces, and the electron velocity is determined directly at the grid cell nodes (Pohjola & Kallio 2010). No macroparticle splitting and joining nor grid refinements are needed because the number of macroparticles and grid cells can be much higher in a parallelized code compared to the earlier sequential code. No predictor–corrector step was used because the time-step was found to be small enough for algorithm stability in the analysed simulation set-up.

2.1 Coordinate system

The planet-centred simulation coordinate system is defined as follows. The x -axis is antiparallel to the incident, undisturbed upstream solar wind flow. The magnetic field of Mercury is represented by a dipole located at the origin with the z -axis along the dipole field perpendicular to the x -axis. The y -axis completes the right-handed coordinate system. The simulation frame approximately corresponds to the frame of a spacecraft orbiting Mercury, because the solar wind flow is much faster than the spacecraft speed with respect to the planet. Thus, we can compare *in situ* measurements, of, e.g. wave polarizations, to the model without additional coordinate transformations. The radius of Mercury is used as the unit of length in some of the figures and text: $R_M = 2439.7 \text{ km}$.

2.2 Description of the run

We analyse a simulation run where the solar wind and IMF conditions are nominal at Mercury's perihelion as estimated by Slavin & Holzer (1981). The incident solar wind ions are mostly protons (H^+) and 4 per cent alphas (He^{++}). The upstream IMF vector is on the xy

Table 1. Numerical simulation set-up and undisturbed upstream solar wind (SW) and IMF conditions at Mercury's perihelion (Slavin & Holzer 1981). The spiral angle is defined as $\arctan(B_y/B_x)$.

Parameter	Symbol	Value
Box size	$x \times y \times z$	$(-10-6 R_M) \times (-8-8 R_M) \times (-8-8 R_M)$
Number of grid cells	$n_x \times n_y \times n_z$	$240 \times 240 \times 240$
Grid cell size	Δx^3	$(163 \text{ km})^3 = (R_M/15)^3$
Number of H^+ macroions	$\mathcal{M}(\text{H}^+)$	139 per cell on average
Number of He^{++} macroions	$\mathcal{M}(\text{He}^{++})$	46 per cell on average
Time-step	Δt	10 ms
SW bulk velocity vector	\mathbf{U}_{sw}	$[v_x = -430 \text{ km s}^{-1}, v_y = 0, v_z = 0]$
SW H^+ temperature	$T_{\text{sw}}(\text{H}^+)$	$1.7 \times 10^5 \text{ K}$
SW He^{++} temperature	$T_{\text{sw}}(\text{He}^{++})$	$6 \times 10^5 \text{ K} = 3.5 T_{\text{sw}}(\text{H}^+)$
SW H^+ density	$n(\text{H}^+)$	73 cm^{-3}
SW He^{++} density	$n(\text{He}^{++})$	$2.92 \text{ cm}^{-3} = 0.04 n(\text{H}^+)$
IMF vector	\mathbf{B}_{sw}	$[B_x = -43.99 \text{ nT}, B_y = 13.45 \text{ nT}, B_z = 0]$
IMF magnitude	$ \mathbf{B}_{\text{sw}} $	46 nT
IMF spiral angle	ϕ	17° (away sector)
Alfvén Mach number	M_A	3.9
Sonic Mach number	M_s	9.0^a
Magnetosonic Mach number	M_{ms}	3.6^a
Plasma beta	β	0.23^a
Dipole ($x = R_M, y = 0, z = 0$)	\mathbf{B}_{dip}	$[B_x = 0, B_y = 0, B_z = 190 \text{ nT}]$
Core radius	R_η	$1800 \text{ km} = R_M - 639.7 \text{ km}$
Core resistivity	$\eta_a(r < R_\eta)$	0
Plasma resistivity	$\eta_a(r \geq R_\eta)$	$7 \times 10^{-3} \mu_0 \Delta x^2 / \Delta t$
Particle absorption radius	R_p	$2439.7 \text{ km} = R_M$

^aNote on the calculation of the sonic and magnetosonic Mach numbers and plasma beta: we assume the polytropic index of $\gamma = 5/3$ and have pressureless (zero temperature) electron fluid in the model.

plane and is assumed to have a nominal Parker spiral ‘away from the Sun sector’ configuration. See Table 1 for the detailed numerical set-up and upstream conditions of the simulation run.

The magnitude of the planetary dipole field is set as 190 nT at the equatorial surface (Anderson et al. 2011; Hauck et al. 2013). We do not consider the displacement of the Hermean dipole field northwards or other non-axially symmetric inner boundary conditions. Further, we do not consider the aberration of the solar wind flow on the xy plane caused by the orbital motion of Mercury around the Sun. The aberration would be $\tan^{-1}(U_{\text{orbit}}/|U_{\text{sw}}|) \approx \tan^{-1}(59 \text{ km s}^{-1}/430 \text{ km s}^{-1}) \approx 7.8^\circ$ in our simulation case. Omitting the dipole displacement and the aberration simplifies the analysis, as any hemispheric asymmetries in the simulation results are due to the solar wind interaction processes rather than asymmetric input conditions to the model. Taking the aberration into account would change the upstream IMF B_x and B_y components by a small amount. The dipole displacement and the aberration are not expected to affect the conclusions of this study. All macroparticles that impact the planet are absorbed by the surface. The core of Mercury is implemented as a superconducting obstacle 640 km below the surface of the planet (see Table 1).

It should be noted that we analyse the Mercury–solar wind interaction using the spatial grid resolution (the side length of cubic grid cells) of 1/15 times the radius of Mercury ($\Delta x \sim 163 \text{ km}$) and at the sampling accuracy of the ion velocity space of ~ 185 macroparticle clouds per cell on average. The spatial grid and velocity resolutions were chosen to allow a large enough simulation domain for a three-dimensional study with available high-performance computing resources. As a comparison, ion scale lengths in the undisturbed solar wind include the thermal gyro

radii of $\sim 15 \text{ km}$ (H^+) and $\sim 29 \text{ km}$ (He^{++}) and the inertial length of $\sim 27 \text{ km}$ (H^+). Any ion physics depending on the electric field, magnetic field, or ion moments at smaller spatial scales than the grid cell size or a finer velocity space sampling than used in the run are not resolved. The ratio of the grid cell size to the ion inertial length is associated with the upper limit of the strength of the electric field Hall term relative to the ion convection term at flow speeds close to the Alfvén velocity (Ledvina et al. 2008). Thus, the grid cell size may affect ion dynamics locally at small scales as we have studied in our earlier hybrid modelling works (Jarvinen et al. 2010, 2014). In the analysed simulation case, it was found that our conclusions presented in this work are not sensitive to the spatial grid resolution (see description of two-dimensional and three-dimensional test runs in the Discussion section). Finally, note that particle motion is not limited to the grid resolution but the macroions move freely inside each cell and from cell to cell, and, for example, undergo gyro motion at the mentioned thermal gyro radius length-scales.

The simulation is initialized with a domain empty of plasma and including only the initial configuration of the magnetic field: the superposition of the planetary dipole field and the IMF flow-aligned component (B_x). The IMF flow-aligned component is implemented as a laminar flow around the inner boundary in the same way as in earlier studies (Shimazu 1999; Kallio, Jarvinen & Janhunen 2006; Jarvinen et al. 2018). The simulation is started by switching on the injection of the solar wind ions from the front wall. The solar wind carries the frozen-in IMF perpendicular component to the flow (B_y), which is held constant in the passive layer of cells (ghost cells) at the front wall. The undisturbed solar wind flows through the simulation box in $16 R_M/V_{\text{sw}} \approx 91 \text{ s}$ (the filling time), and soon after that the simulation was found to reach a quasi-

stationary state of development at $t \sim 130$ s (see Movie S01 in the supplementary material). Note that during the initialization, the constraints described in the previous section prevent the occurrence of anomalously strong electric fields or high signal speeds in empty or very low-density plasma regions. According to our tests, after the initialization the constraints affect the solution only in low-density or high magnetic field strength regions. That is, the roof and floor limits are effective mostly in the magnetotail of Mercury, and we do not expect them to change the foreshock region analysed in this study.

To analyse the upstream plasma waves, particles and fields were recorded at every time-step between $t = 250$ and 450 s in grid cells centred at points P1 ($x = 1.97 R_M$, $y = -2.30 R_M$, $z = 0.03 R_M$) and P2 ($x = 1.97 R_M$, $y = 2.30 R_M$, $z = 0.03 R_M$).

3 RESULTS

Figs 1 and 2 give an overview of different aspects of the interaction between Mercury and the solar wind in the simulation. The morphology of the magnetic field shows the 17° Parker spiral angle in the upstream region and the connection of the upstream IMF to the bow shock and the downstream region and the planet (Fig. 1). The deflection and slowing down of the solar wind flow around the planet results in a formation of the bow shock, where the ion density is highest near the subsolar region (Figs 2a and b). A magnetosheath is formed between the bow shock and the low-density magnetotail region. The magnetosheath is asymmetric between the $y > 0$ (the quasi-perpendicular hemisphere) and $y < 0$ (the quasi-parallel hemisphere) hemispheres due to the Parker spiral IMF configuration.

The quasi-parallel bow shock forms on the $y < 0$ hemisphere. The IMF has a strong S-shaped ‘kink’ or a turning of the B_x component from $B_x < 0$ (away from the Sun) to $B_x > 0$ (towards the Sun) configuration near the quasi-parallel bow shock. On the opposite $y > 0$ hemisphere, the IMF changes only moderately because of piling up and deflection near the quasi-perpendicular bow shock. On the night side of the planet, a low-density wake, or a magnetotail, is created, where no or only few upstream IMF lines connect. Note that the three-dimensional field line tracing was started on the $z = 500$ km plane upstream of the bow shock in Fig. 1. In the downstream region, the field lines move upwards and some of them connect to the planet’s dipole field and surface on the northern ($z > 0$) hemisphere. On the quasi-perpendicular hemisphere, the IMF does not connect near to the planet but to the magnetosheath. The solar wind flow slows down more in the magnetosheath on the quasi-parallel hemisphere as compared to the quasi-perpendicular hemisphere (Fig. 2a).

The proton temperature shows an asymmetric increase at the bow shock between the $y > 0$ and $y < 0$ hemispheres on the $z = 0$ plane (Figs 1 and 2c and d) with respect to the undisturbed solar wind proton temperature. On the $y > 0$ hemisphere, the temperature increases when moving from the upstream region to the bow shock and to the magnetosheath. On the quasi-parallel $y < 0$ hemisphere, a significant increase in the proton temperature is seen already upstream of the bow shock. We refer to the upstream region with increased ion temperature as the ion foreshock or simply as the foreshock in this work.

Waves with large spatial scales form in the magnetic field in the foreshock hemisphere, whereas on the opposite hemisphere there is no significant wave activity upstream of the quasi-perpendicular bow shock (Figs 2e–f). The foreshock waves fluctuate on both sides of the undisturbed IMF B_y value with similar amplitudes. The

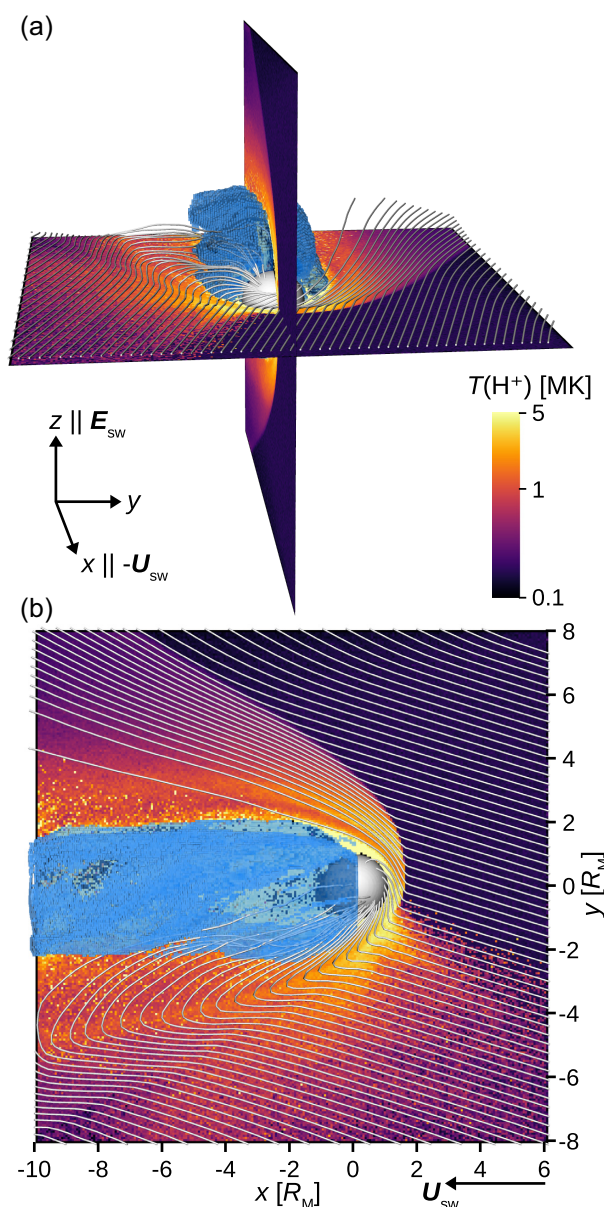


Figure 1. Overview of the magnetic field lines connected to the upstream region and the proton temperature in the analysed Mercury simulation run at $t = 350$ s. (a) The top panel shows a three-dimensional view and (b) the lower panel shows a view towards the $z = 0$ plane. The temperature is shown on the xy ($z = 0$) and xz ($y = 0$) planes. Three-dimensional magnetic field line tracing was started in the upstream region on the $z = 500$ km plane. The blue volumetric plot shows the region where the total ion density is 10 cm^{-3} or below in the magnetotail. The black arrows give the orientation of the coordinate axes and the undisturbed upstream solar wind bulk velocity (U_{sw}) and convection electric field (E_{sw}) vectors.

increased proton temperature and the B_y wave activity both have a cut-off near the subsolar region on the quasi-parallel hemisphere on the field line with $\theta_{Bn} \sim 0$. We call this the ion foreshock boundary in the simulation.

The structure of the ion foreshock perpendicular to the $z = 0$ plane (along the IMF vector) is shown for context in the insets of Figs 2(b), (d), and (f). It can be seen that the foreshock extends from $z \sim -1.0$ to $z \sim 1.5 R_M$. Fig. 2b shows density enhancement at the edges of the ion foreshock (Fig. 2b). The density enhancement is

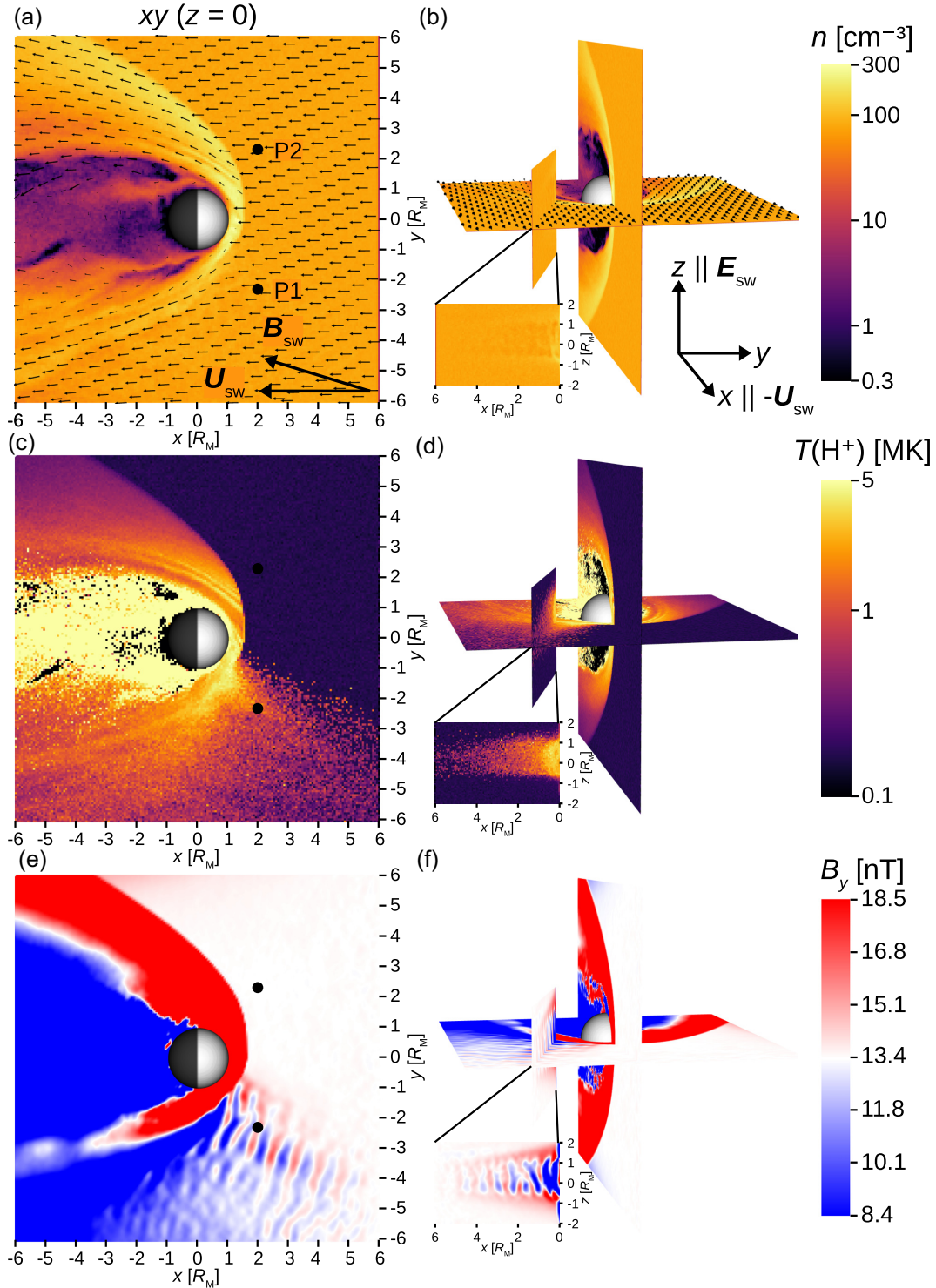


Figure 2. Overview of the plasma properties in the analysed Mercury simulation run at $t = 350$ s. (a,b) The top panels show the total ion density (n) at the xy ($z = 0$) and xz ($y = 0$) planes with the structure of the foreshock perpendicular to the xy plane displayed on an inclined slice oriented along \mathbf{B}_{sw} . The ion bulk velocity vectors are shown in black on the xy plane with the maximum vector length limited at twice the upstream undisturbed solar wind speed. (c,d) The middle panels display the proton scalar kinetic temperature ($T(H^+)$) in the same format as the top panels. (e,f) The bottom panels show the B_y component of the magnetic field in similar format as the top panels. Note that n and B_y are temporal averages over 20 time-steps (0.2 s) whereas $T(H^+)$ is a snapshot value. A red–blue difference colour map is chosen in panels (e,f) to visualize fluctuations centred around the undisturbed upstream B_y value, which correspond to the white colour. Points P1 and P2 mark the locations of the simulation cells that are used to analyse plasma temporal properties in this work. The thick black arrows in panels (a,b) give the orientation of the coordinate axes and the following vectors in the undisturbed upstream region: the solar wind bulk velocity (\mathbf{U}_{sw}), the interplanetary magnetic field (\mathbf{B}_{sw}), and the convection electric field (\mathbf{E}_{sw}).

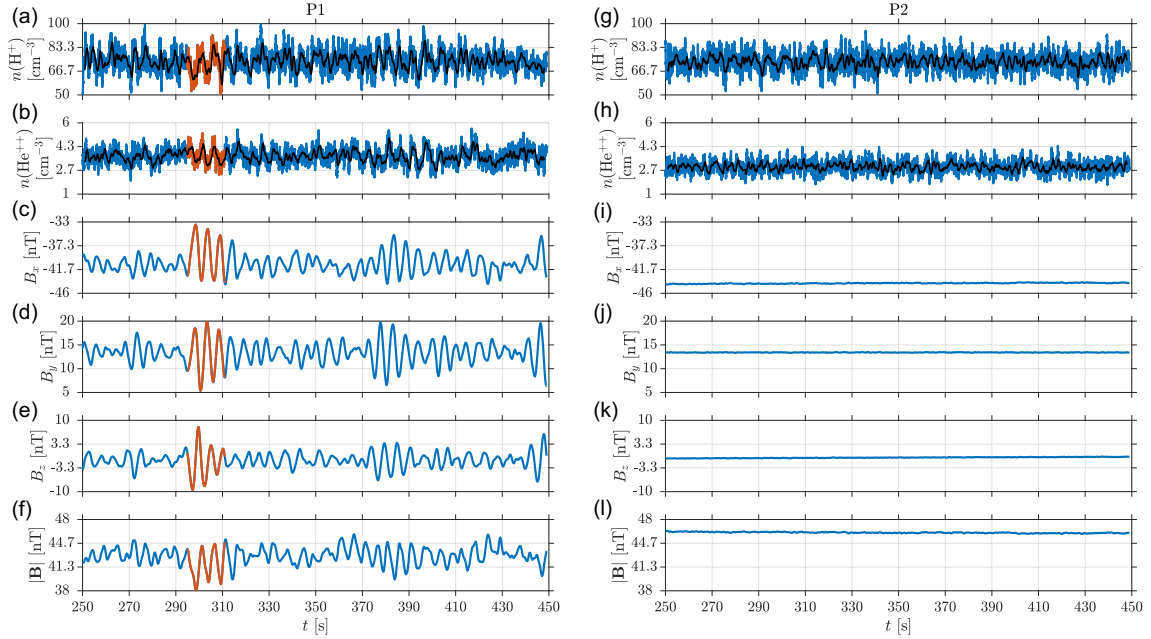


Figure 3. Time series of ion densities and magnetic field at P1 and P2 shown in Fig. 2. Panels from the top are: (a/g) H^+ density, (b/h) He^{++} density, (c/i) B_x component of the magnetic field, (d/j) B_y component of the magnetic field, (e/k) B_z component of the magnetic field, and (f/l) magnitude of the magnetic field. Black curves in the density panels give the densities with the running average over 1 s. Further analysis of the wave mode is done in the period plotted in red at P1.

strongest and the foreshock proton temperature highest (Fig. 2d) near the bow shock. The dynamics of the total ion density and B_y on the $z = 0$ plane during the simulation run is available in the supplementary material Movie S01.

Fig. 3 shows the time series of the H^+ and He^{++} densities and the magnetic field at two points symmetrically placed upstream of the bow shock on opposite hemispheres of the $z = 0$ plane. The point P1 is in the foreshock and the point P2 is in the quasi-perpendicular hemisphere. Large-scale foreshock fluctuations are seen in the densities and in all the components and magnitude of the magnetic field at P1. The wave activity occurs at the period of few seconds throughout the interval. The maximum peak-to-peak amplitude is about $\delta B/B = 16$ per cent. Modulations of the magnetic field components show two ‘wave trains’ lasting ~ 40 s each ($t = 290\text{--}330$ s and $t = 370\text{--}410$ s). In the quasi-perpendicular hemisphere, no upstream large-scale magnetic wave activity is seen.

Fig. 4 shows the temporal properties of the H^+ and He^{++} species summed together as well as the B_y component at P1 and P2. The upstream solar wind beams are seen in the ion time–energy spectra in the top panels at both points. The proton beam is centred at ~ 1 keV and the alpha beam at ~ 4 keV as expected. At P1, there are scattered ions at higher and lower energy sides of the solar wind beams with energies reaching above 10 keV and below 100 eV. On the other hand, there are almost no ions outside of the solar wind beams at P2. Note that zooming in the figure to the beams reveals \sim second-scale fluctuations in the foreshock, whereas no fluctuations of the beams are evident on the quasi-perpendicular hemisphere.

Temporal evolution of the wave activity of the density and B_y are analysed by wavelet transformations in Figs. 4(b), (d), (g), and (i). The main difference in the frequency–domain plots between the points P1 and P2 is the strong spectral power at the period of ~ 5 s (0.2 Hz) in the foreshock. We refer to this as the 5-s wave, mode, or peak in this study. The spectral peak is pronounced in B_y but also

clear in the density at P1. The strongest period of the 5-s spectral power in the foreshock is associated with the two ‘wave trains’. B_y does not have significant power at other frequencies than 5 s. The overall B_y spectral power is orders of magnitude less powerful at P2 as compared to P1.

Fig. 5 shows Fourier spectra of the density and B_y for the total time period of Fig. 3 ($t = 250\text{--}450$ s). The 5-s peak is clear in the B_y spectrum and also visible in the density spectrum at P1. The P1 spectral power decreases for both quantities when moving away from the 5-s maximum, whereas at P2 the spectral power is quite flat for frequencies below half a hertz. The running average gives the peak period range of 4.8–5.3 s (0.19–0.21 Hz) at P1. The comparison of the Fourier spectra shows again that the overall spectral power of the magnetic field is orders of magnitude less in the quasi-perpendicular upstream region compared to the foreshock.

Fig. 6 gives the velocity distribution of H^+ and He^{++} ions within the simulation cell at the foreshock point P1. The main solar wind beams are visible as nearly spherically symmetric populations centred at nearly undisturbed upstream velocity. The reflected ion populations are seen as wider distributions located at velocities away from the solar wind beams in the direction antiparallel to the magnetic field. The foreshock populations are centred around the magnetic field vector and roundish arcs in the foreshock populations in panels (c) and (d) occur because of ion gyro motion around the magnetic field. Each arc forms when a single macroparticle travels through the simulation cell centred at P1 and gyrates over a range of gyrophases.

Fig. 7 shows time–energy spectrogram and density of the foreshock ions at P1. The foreshock ions were selected from the whole ion distribution by including only the ions away from the solar wind population. We estimate that the solar wind beam population includes all particles within the sphere of radius 250 km s^{-1} centred at U_{sw} (value listed in Table 1) in the velocity space (Fig. 6).

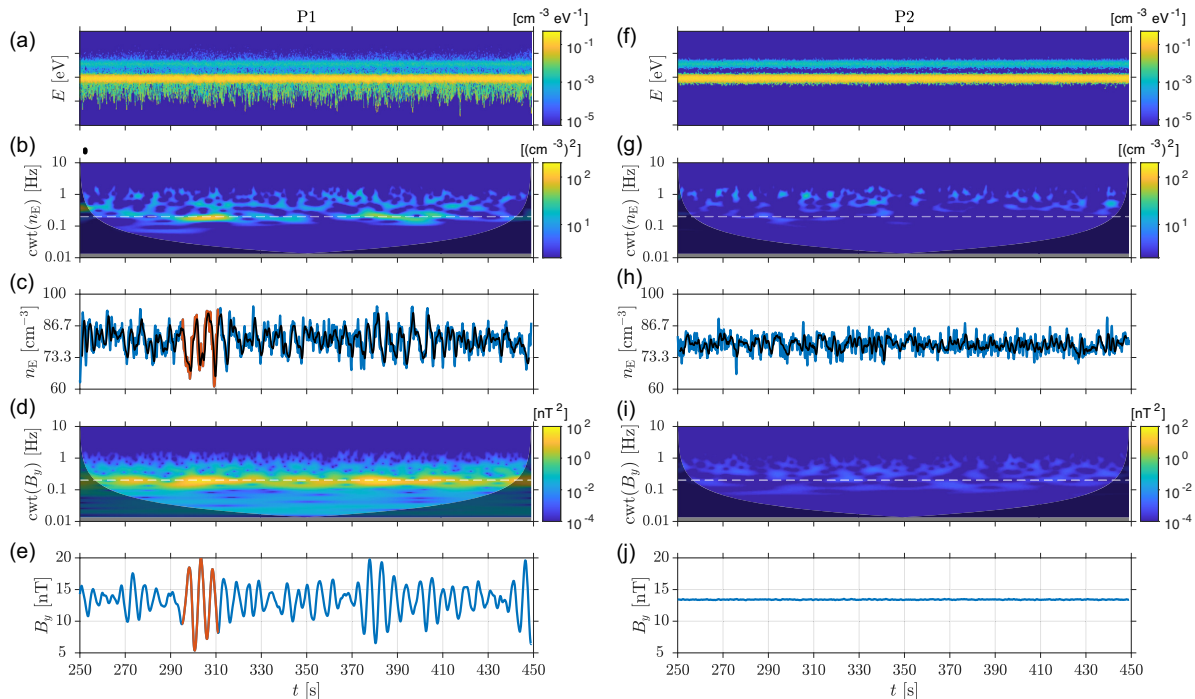


Figure 4. Time series of ion and magnetic field parameters at P1 and P2. Panels from the top are: (a/f) omnidirectional ion time–energy spectra, (b/g) wavelet power spectrum (continuous wavelet transformation) of electron density, (c/h) electron density, (d,i) wavelet power spectrum (continuous wavelet transformation) of B_y component of the magnetic field, and (e/j) B_y component of the magnetic field. (a/f) The omnidirectional time–energy ion spectra were determined as $\sum_i w_i / (\Delta V \Delta E)$, where the summation i is over macroparticles in a grid cell (ΔV is the cell volume), the energy range per bin is $[E, E + \Delta E]$, and w_i is the statistical weight of a macroparticle. 99 energy bins were used and they were logarithmically spaced from 10 to 80 keV. (b, d, g, and i) Dashed white horizontal lines denote the period (frequency) of 5 s (0.2 Hz). The spectra in panels (a/f) are binned using a temporal average over 20 time-steps (0.2 s) whereas other panels have full temporal resolution. The black curves in the density panels give the densities with the running average over 1 s. Further analysis of the wave mode is done in the period plotted in red at P1.

Consequently, the foreshock population includes only particles outside of the sphere of radius 250 km s^{-1} centred at U_{sw} . We call these ions the suprathermal population or, in general, the suprathermal foreshock population or just the foreshock population. Further, we refer to the part of the suprathermal population with $v_x > 0$ as the backstreaming (foreshock) ions.

The time–energy spectrogram shows that the foreshock H^+ and He^{++} populations have a wider spread in kinetic energy compared to the solar wind beams. Further, it is interesting to note that the foreshock population has fluctuations at \sim second to few-second periods. The ratio of the suprathermal ion density to the total density of the species fluctuates around the average value of 6 per cent for H^+ and around the value of 25 per cent for He^{++} at P1. We also derived the average ratio of backstreaming ions to the total density of the species, which is 5 per cent for H^+ and 18 per cent for He^{++} at P1 (figure not shown). About 7 per cent (6 per cent) of the total ion number density and about 9 per cent (7 per cent) of the total ion mass density are in the suprathermal (backstreaming) ions. There are no suprathermal or backstreaming ions at P2.

Fig. 8 displays the minimum variance analysis (MVA) (Sonnerup & Scheible 1998) of the first wave train at P1 over a period of 16 s ($t = 295\text{--}311$ s). The unit vector \hat{k} (Fig. 8c) is an estimation of the orientation of the wave vector, where we have fixed the sign of \hat{k} by the fact that the waves convect along rather than antiparallel to the solar wind flow in the simulation frame (see Movie S01 in the supplementary material). The eigenvalue of the minimum variance direction is more than an order of magnitude smaller than the eigenvalues of the intermediate and maximum variance

directions implying a good MVA solution. The hodograms show the same: the periodic (5-s) wave motion is evident on the plane of the maximum and intermediate variances. The angle between the average magnetic field during the interval and the wave vector is about $\cos^{-1}(\hat{b} \cdot \hat{k}) = 23.7^\circ$. Note that the average unit magnetic field vector is close to the direction of the undisturbed IMF ($\sim 3.3^\circ$ difference) as expected in the upstream region. Fig. 8e shows that the 5-s waves are polarized in a left-handed sense with respect to the magnetic field in the simulation frame.

Fig. 9 gives the Fourier spectra of the magnetic field along and perpendicular to the direction of the wave propagation as determined by the MVA analysis. The spectra show that the wave power in the magnetic field component along the wave propagation is overall less than in the transverse component. The transverse spectrum shows the peak at the frequency of 0.19 Hz (5.3 s), which is the maximum wave power density.

Fig. 10 shows a correlation analysis of the electron density and the magnitude of the magnetic field at P1 during the same interval as Figs 8 and 9. The correlation is strongly positive with the Pearson correlation coefficient of 0.84.

4 DISCUSSION

We demonstrate the existence of an ion foreshock and large-scale ULF foreshock wave activity at Mercury in a three-dimensional hybrid simulation. A portion of the incident solar wind ion flux is scattered back upstream near the quasi-parallel bow shock. The upstream conditions correspond to nominal solar wind and IMF at

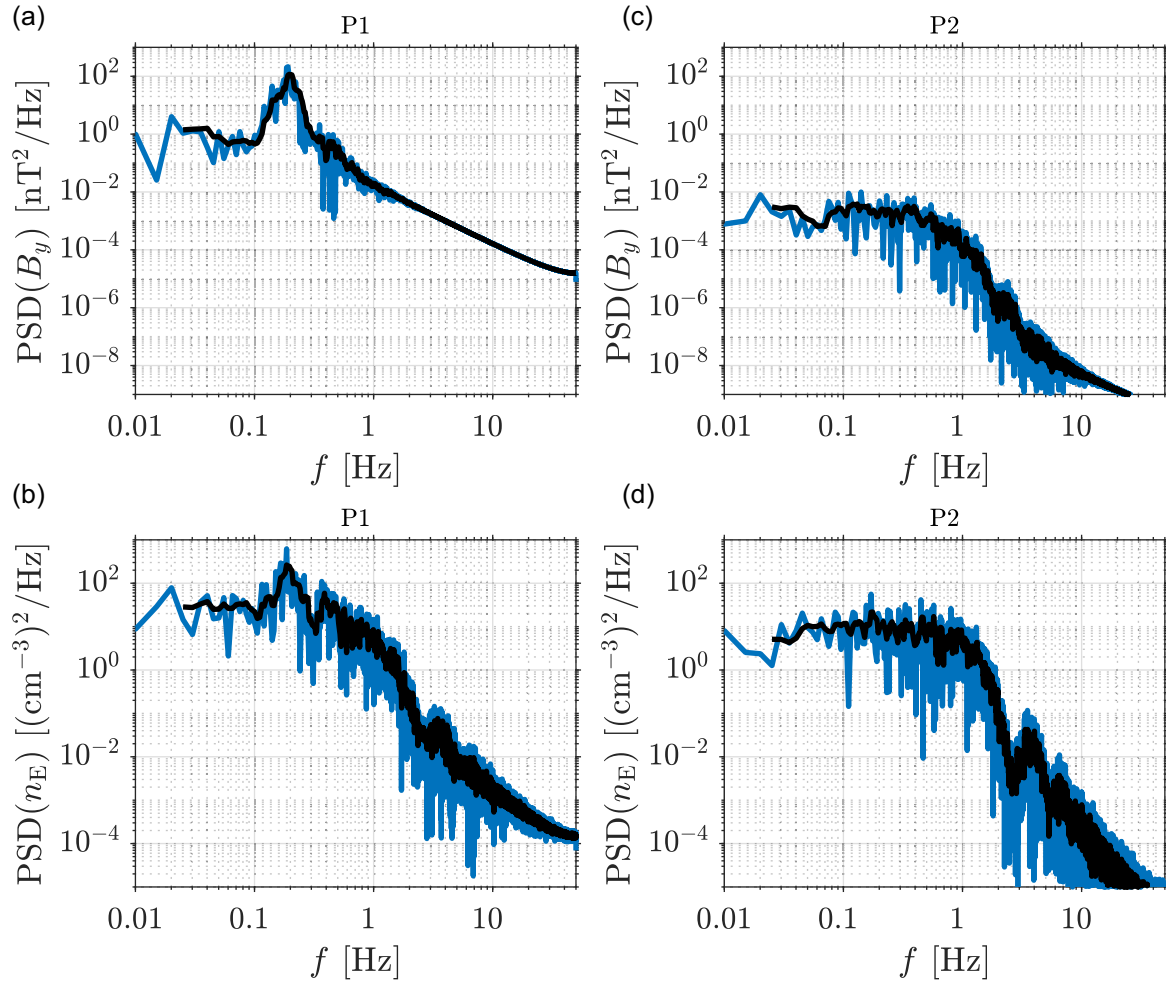


Figure 5. Power spectral density (PSD) of the (a/c) B_y component of the magnetic field and (b/d) electron density at points P1 and P2 in the period of $t = 250\text{--}450$ s. The plots were computed as the fast Fourier transforms of the corresponding time series in Fig. 4. The black curves give running averages of the spectra over five frequency bins.

the planet’s orbital perihelion. In the foreshock, the waves at the period of $\sim 4.8\text{--}5.3$ s (0.19–0.21 Hz), which we refer to as the 5-s waves in this study, are pronounced and dominate the spectral power of both the magnetic field and the plasma density.

The properties of the 5-s waves include positive correlation of the density and the magnitude of the magnetic field. Further, according to the MVA analysis, the 5-s waves are left-hand polarized and travel at the angle of 23.7° with respect to the magnetic field in the simulation frame. The peak-to-peak amplitude reaches the maximum value of $\delta B/B \sim 16$ per cent and the waves are moderately compressional. Taken together, these features are in agreement with the 0.3 Hz (3.3 s) fast-mode magnetosonic waves propagating obliquely with respect to the background magnetic field as observed upstream of the Hermean bow shock (Fairfield & Behannon 1976; Le et al. 2013).

An accurate, direct estimation of the wave velocity in the simulation is a challenging task, because the foreshock plasma and the ULF wave pattern are both spatially and temporally variable. The velocity of the wave phases depends on the wavelength (λ_w) and the wave frequency (f) as $v_p = \lambda_w f$. The wavelength can be determined from a snapshot state of the simulation (spatial method), from temporal evolution of the simulation (temporal method) or as a combination of these two. The PSD in Figs 5 and 9 gives the main

wave frequency. We estimate the phase velocity of the 5-s modes using the spatial method as follows.

The wavelength was determined from a magnetic field profile along a $2 R_M$ long line centred at P1 in the direction of \hat{k} at $t = 303$ s (the middle of the MVA analysis period). Peak-to-peak distances of magnetic field maxima were measured separately for B_i and B_j components. The distances between the nearest peaks to P1 are in the range of $\lambda_w = 1525\text{--}1720$ km. These wavelengths are associated with the range of $v_p = 290\text{--}327$ km s $^{-1}$ phase velocities along \hat{k} at the frequency of $f = 0.19$ Hz, which is the peak ULF PSD over the whole analysed 200-s period (Fig. 5) as well as over the 16-s MVA period (Fig. 9).

Fig. 11 shows the bulk velocity of the solar wind beam population (U_{beam}) projected along the \hat{k} vector at P1. The bulk velocity of the solar wind beam was determined as a mass-weighted average velocity including both the solar wind protons and alphas. It can be seen from the figure that the solar wind beam is travelling along \hat{k} at speeds on average faster than the estimated maximum ULF phase velocity. Thus, we conclude that the ULF waves are propagating upstream in the frame of the solar wind beam and undergo the polarization change from the intrinsic right-handed polarization to the left-handed polarization observed in the simulation frame due to the Doppler shift (Fairfield & Behannon 1976; Le et al. 2013).

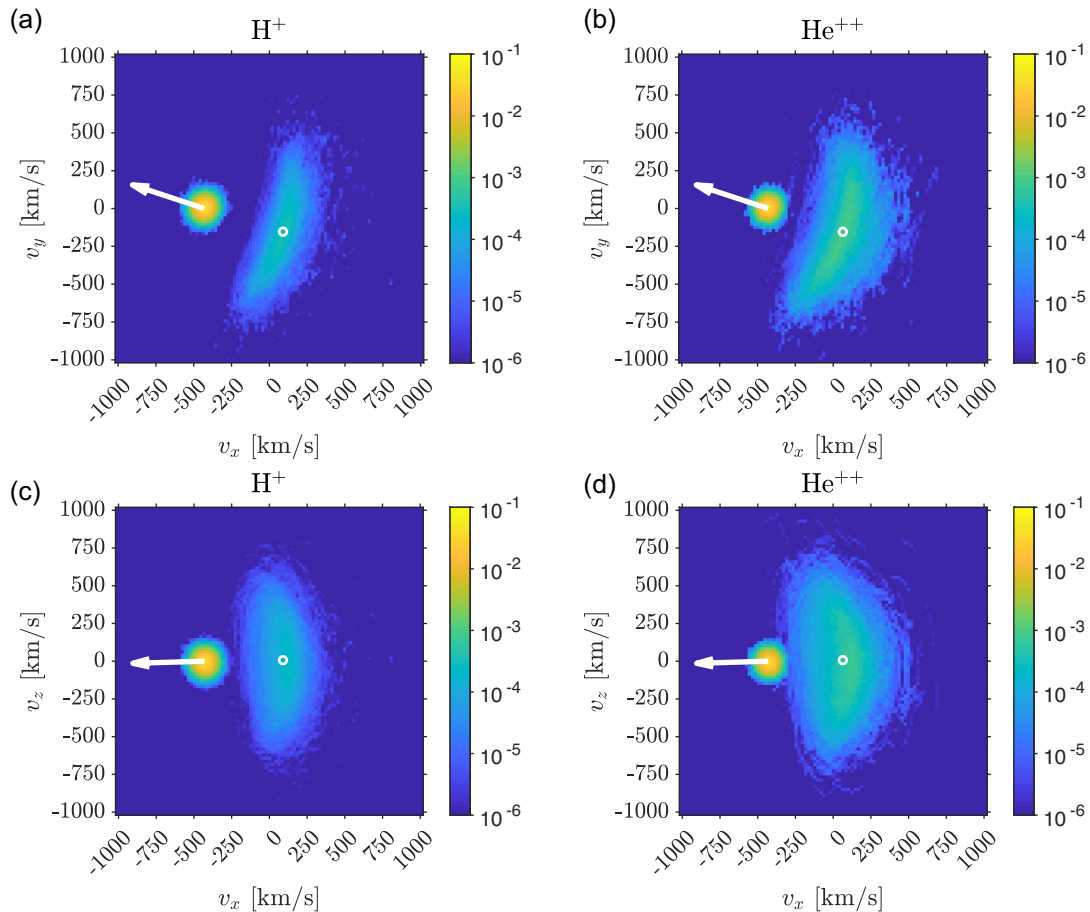


Figure 6. Velocity distributions of (a/c) H^+ and (b/d) He^{++} ions in the period of $t = 250\text{--}450$ s at P1. The plots are projections of the whole three-dimensional velocity distribution collapsed on the (v_x, v_y) and (v_x, v_z) planes. The white arrows show the orientation of the average magnetic field vector projected on the planes over the same time period. The starting point of the white arrows is the undisturbed upstream bulk velocity (\mathbf{U}_{sw} in Table 1). The white circles give the bulk velocity of the suprathermal foreshock ion populations. The colouring gives the number of particles in each velocity bin divided by the total number of particles in the panel.

An interesting question is how the frequency of the Hermean foreshock ULF waves relates to other planets. At Earth, the common 30-s (0.033 Hz) foreshock waves have similar properties as the fast magnetosonic waves in the Hermean foreshock (Le et al. 2013). Scaling the wave period by the IMF strength (or the gyro frequency) gives the correspondence of the 30-s waves at Earth ($B = 6$ nT) to 3.9 s (0.26 Hz) at Mercury’s perihelion ($B = 46$ nT) (Hoppe & Russell 1982). This is close to the period of the 5-s waves in our simulation case. The magnetosonic foreshock ULF waves occur also at Venus (Russell & Hoppe 1983; Orłowski et al. 1995) mainly at the periods $\sim 20\text{--}30$ s (0.033–0.05 Hz) (Shan et al. 2016). These correspond to the periods of 4.3–6.5 s (0.15–0.23 Hz) when scaled by the IMF strength ratio at Venus to Mercury’s perihelion (10/46 nT). This is also close to the periods of the 5-s waves in our simulation case. As a further comparison, the gyro periods of protons and alphas are 1.4 s (0.71 Hz) and 2.8 s (0.36 Hz), respectively, in the undisturbed solar wind in our simulation case. The frequency of the 5-s foreshock waves is below the ion gyro frequencies.

Note that Mercury and MESSENGER were at about 0.34 au distance from the Sun during the observed ~ 0.3 Hz ULF fast-mode waves (Le et al. 2013). At this distance, the average solar wind density is about 83 percent of its Hermean perihelion

value (Slavin & Holzer 1981) meaning that the bow shock may have been somewhat further away from the planet during the observation than in our simulation case. The planetocentric distance of MESSENGER from Mercury was about $5.5 R_M$ during the observation, whereas the foreshock point P1 is at the planetocentric distance of $3.0 R_M$. This can contribute to our waves being slightly stronger in $\delta B/B$ amplitude than the observed ones. The IMF strength during the observation was ~ 31 nT. According to the scaling discussed above, the waves observed by MESSENGER correspond to $0.3 \text{ Hz} \times 31 \text{ nT}/46 \text{ nT} \approx 0.20 \text{ Hz}$ (5 s) waves in our Mercury perihelion case, which is within the frequency range of the 5-s modes in the simulation.

The ion velocity distribution in Fig. 6 shows two distinct particle populations in the foreshock at P1. The bulk velocity of the solar wind beam populations for both solar wind species is $\mathbf{U}_{\text{beam}} = (v_x = -427 \text{ km s}^{-1}, v_y = 7 \text{ km s}^{-1}, v_z = -4 \text{ km s}^{-1})$ averaged over the whole 200-s analysis period. That is, $\mathbf{U}_{\text{beam}} \sim \mathbf{U}_{\text{sw}}$ (Table 1) and the foreshock processes have not slowed down or changed the direction of the solar wind beam considerably at the $3 R_M$ planetocentric distance. However, as Fig. 11 shows, the bulk velocity of the solar wind beam population shows small variations at a similar period than the 5-s ULF waves. Thus, hints of the foreshock ULF wave activity can be observed by analysing the solar wind beam alone

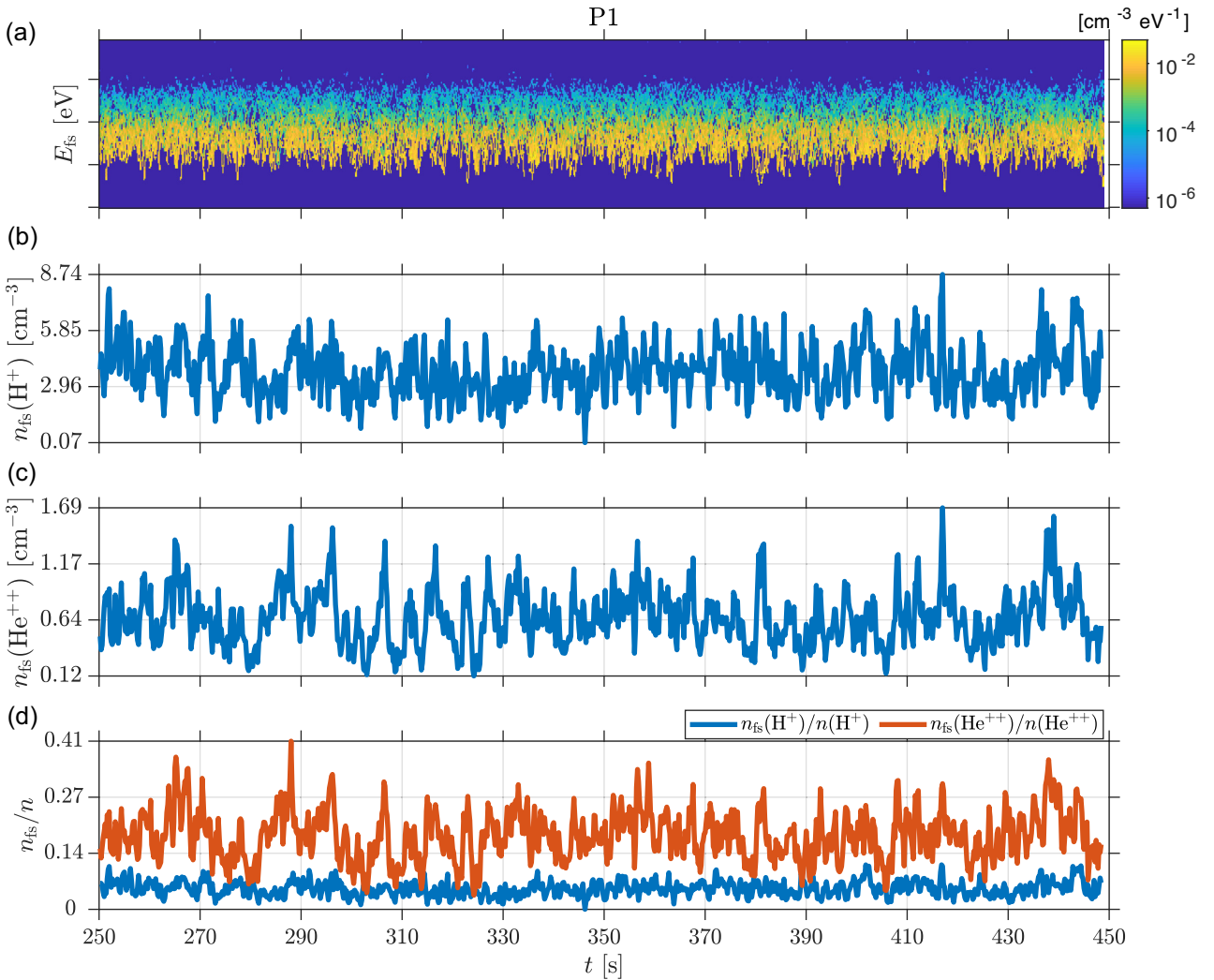


Figure 7. Time series of the suprathermal foreshock (fs) ion properties at P1. Panels from the top are: (a) the omnidirectional suprathermal ion time–energy spectra, (b) the density of suprathermal H^+ ions, (c) the density of suprathermal He^{++} ions, and (d) the density of suprathermal H^+ and He^{++} ions divided by the total ion density per corresponding species. The spectra in panel (a) is binned using a temporal average over 20 time-steps (0.2 s) in the same way as the spectra in Figs 4(a) and (f) whereas other panels have full temporal resolution. The black curves give running averages of the quantities over 1 s.

provided that a particle instrument has good enough energy and angular resolution.

The second population is the suprathermal foreshock population, which is located away from the solar wind beam in the direction antiparallel to the magnetic field and has a much wider spread in velocities than the solar wind beam. The bulk velocities of the foreshock populations in Fig. 6 are $\mathbf{U}_{fs}(H^+) = (v_x = 90 \text{ km s}^{-1}, v_y = -153 \text{ km s}^{-1}, v_z = 7 \text{ km s}^{-1})$ for protons and $\mathbf{U}_{fs}(He^{++}) = (v_x = 64 \text{ km s}^{-1}, v_y = -154 \text{ km s}^{-1}, v_z = -6 \text{ km s}^{-1})$ for alphas. These are less than a half of the bulk speed of the solar wind beam.

In order to analyse the formation of the foreshock population, we released test particles in the model. In the test particle tracing, ions were initially positioned in the upstream region just ahead of the quasi-parallel bow shock on the $z = 0$ plane at $x = 2R_M$ and $y = -0.5$ – $4.0 R_M$. Each initial (x, y, z) point included a set of test particles with the initial velocities ranging from -150 to 150 km s^{-1} from the undisturbed solar wind bulk velocity in all three velocity components. The particles were propagated using the Lorentz force in stationary, three-dimensional electric and magnetic fields at $t = 350 \text{ s}$. About 24 000 test particles of both species were

released and most of them pass the bow shock and keep moving in the downstream magnetosheath. However, a portion of the test ions are energized and scattered near the quasi-parallel bow shock. As a result, some of these particles gain a velocity vector with $v_x > 0$ and, thus, move back in the upstream region forming the foreshock population.

Fig. 12 shows example trajectories of the foreshock ions from the test particle tracing. It can be seen that the backstreaming ions are started from the y coordinate range of about $y = -0.5$ – $2.5 R_M$. At the shock, each y coordinate corresponds to a θ_{Bn} angle. The y coordinate range of the backstreaming ions corresponds to about $\theta_{Bn} = 0$ – 52° . Note that only a portion of the ions started at the mentioned y and θ_{Bn} range are reflected depending on their initial velocity. Reflected alphas have a somewhat wider range of initial y and θ_{Bn} than protons suggesting charge-to-mass ratio dependence in the reflection. Exact criteria for the solar wind ion reflection associated with the Hermean quasi-parallel bow shock should be quantified in future studies.

In Earth’s ion foreshock, several types of suprathermal ion distributions have been observed (see, for example, reviews by

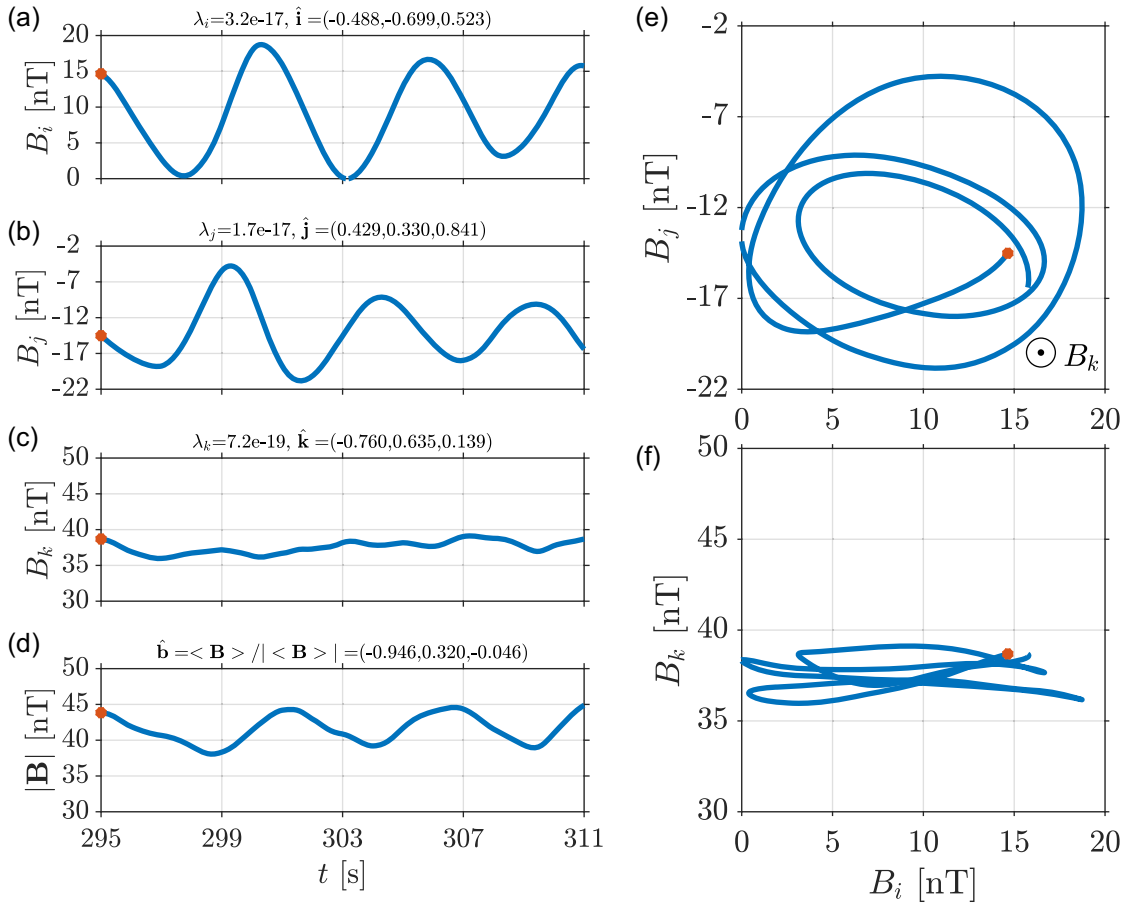


Figure 8. MVA of the magnetic field at P1 in the period of $t = 295$ – 311 s. (a–c) Left-hand panels show the components of the magnetic field in the MVA coordinate system. In the left-hand panel titles, λ_i , λ_j , and λ_k give the eigenvalues of the magnetic variance matrix and \hat{i} , \hat{j} , and \hat{k} are the unit vectors of the maximum, intermediate, and minimum variance directions in the simulation coordinate system, respectively. The title of panel (d) gives the unit vector of the average magnetic field ($\hat{\mathbf{b}}$) in the simulation coordinate system in the MVA analysis period. (e) The hodogram of the magnetic field on the plane of the maximum and intermediate variance directions. (f) The hodogram of the magnetic field on the plane of the maximum and minimum variance directions. The red dots denote the start of the time series.

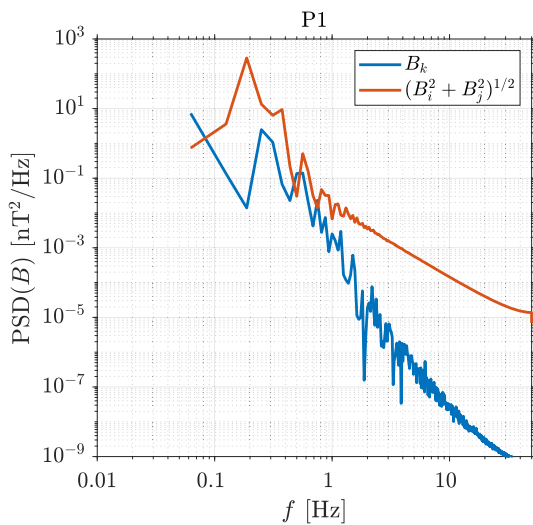


Figure 9. PSD of the magnetic field in the MVA coordinate system at P1 in the period of $t = 295$ – 311 s.

Fuselier 1994; Eastwood et al. 2005; Burgess, Möbius & Scholer 2012, and references therein). The 30-s ULF waves are often associated with the so-called intermediate ion distributions (Hoppe et al. 1981; Paschmann et al. 1981; Fuselier et al. 1986). These and the field-aligned beam ion distributions (Asbridge, Bame & Strong 1968) are wide in velocities and located away from the solar wind beam in the direction aligned (or antiparallel) with the magnetic field. The Hermean foreshock population in Fig. 6 is also located away from the solar wind beam in the direction antiparallel to the magnetic field. However, the intermediate and field-aligned beam distributions are located at velocities higher than the solar wind beam at Earth, whereas the foreshock population in our model run has a bulk velocity less than a half of the solar wind beam and a part of the distribution has $v_x \sim 0$. Thus, the formation mechanism of the foreshock population in Fig. 6 likely differs from Earth’s foreshock. The formation of the intermediate distributions is often associated with the field-aligned beams, originated at the quasi-perpendicular bow shock, undergoing wave–particle interactions and travelling upstream to the quasi-parallel bow shock region of Earth (for example, Fuselier 1995; Eastwood et al. 2005). In our simulation case, the Hermean foreshock population forms via scattering near the quasi-parallel shock as seen by test particle tracings described above. Processes at Earth’s quasi-parallel bow shock

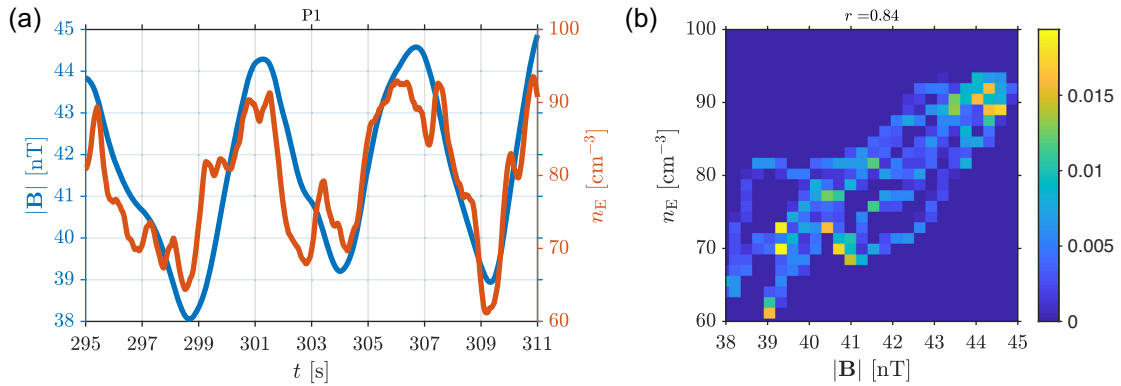


Figure 10. Correlation of the electron density and the magnitude of the magnetic field at P1 in the period of $t = 295\text{--}311$ s. (a) The left-hand panel shows time series of the parameters. (b) The right-hand panel gives the probability density map and the Pearson correlation coefficient (r) of the parameters.

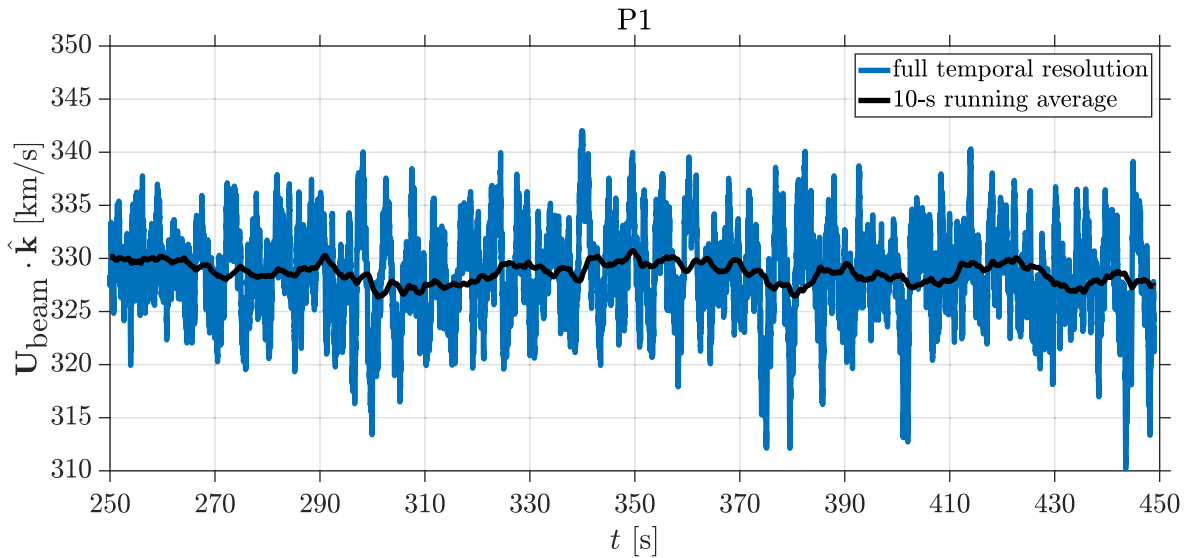


Figure 11. Time series of the bulk velocity of the solar wind beam (U_{beam}) projected along the unit vector \hat{k} determined by the MVA at P1. The blue curve has the full temporal resolution and the black curve is the running average over 10 s.

include specular reflection, which is associated with the gyrophase-bunched and diffuse distributions (Gosling et al. 1982; Paschmann et al. 1982). We do not observe these types of distributions near the quasi-parallel shock in the model. However, backstreaming ions near the ion foreshock boundary [see sporadic high temperatures at $(x > 2R_M, y \sim -2\text{--}0R_M)$ in Figs 1b and 2c] seem to occur at higher velocities than at P1, which could be related to a field-aligned population-type distribution. All in all, a detailed study of ion scattering and acceleration mechanisms at the Hermean bow shock under different upstream conditions and Mach numbers as well as foreshock ion velocity distributions based on models and observations is called for in future works.

We performed several test runs to investigate if our conclusions presented in this study are sensitive to the model set-up. In a three-dimensional grid resolution test, we use the same simulation set-up of 17° Parker spiral case as analysed here except that the upstream IMF magnitude is only 7 nT and the upstream ion densities are set such that the Mach numbers remained unchanged with 4 per cent of alphas. The lower IMF strength and density mean that the upstream ion gyro radius to the grid cell size ratio ($r_L/\Delta x$) and the upstream ion inertial length to the grid cell size ratio ($d_i/\Delta x$)

are increased by the factor of ~ 6.6 . It was found that the Hermean foreshock included fast-mode ULF waves in this test run with a similar absolute magnitude (δB) as in the analysed 46-nT run, but, as expected by the scaling of Hoppe & Russell (1982) discussed above, at the longer wave period of $\sim 25\text{--}50$ s ($\sim 0.02\text{--}0.04$ Hz).

The grid resolution testing was continued with a two-dimensional run with the grid cell size of $\Delta x = 12.7$ km. In this test, the simulation configuration and the upstream conditions are the same as in the three-dimensional Mercury perihelion case, except that the simulation domain is only the $y < 0$ region on the day side of the xy plane (the foreshock side), the z direction is periodic, and the time-step (Δt) is decreased such that $\Delta x/\Delta t$ remains constant. The $r_L/\Delta x$ and $d_i/\Delta x$ ratios are above unity and increased by the factor of ~ 12.8 compared to the analysed three-dimensional run. It was found that the ion foreshock in the two-dimensional test includes ULF waves at the period of ~ 5 s and at a similar magnitude as in the analysed three-dimensional run and the waves are left-hand polarized fast modes in the simulation frame. Thus, our conclusions presented in this study are not sensitive to the grid resolution.

Another test was performed using a free-flowing solar wind through an empty simulation domain. The empty box run was

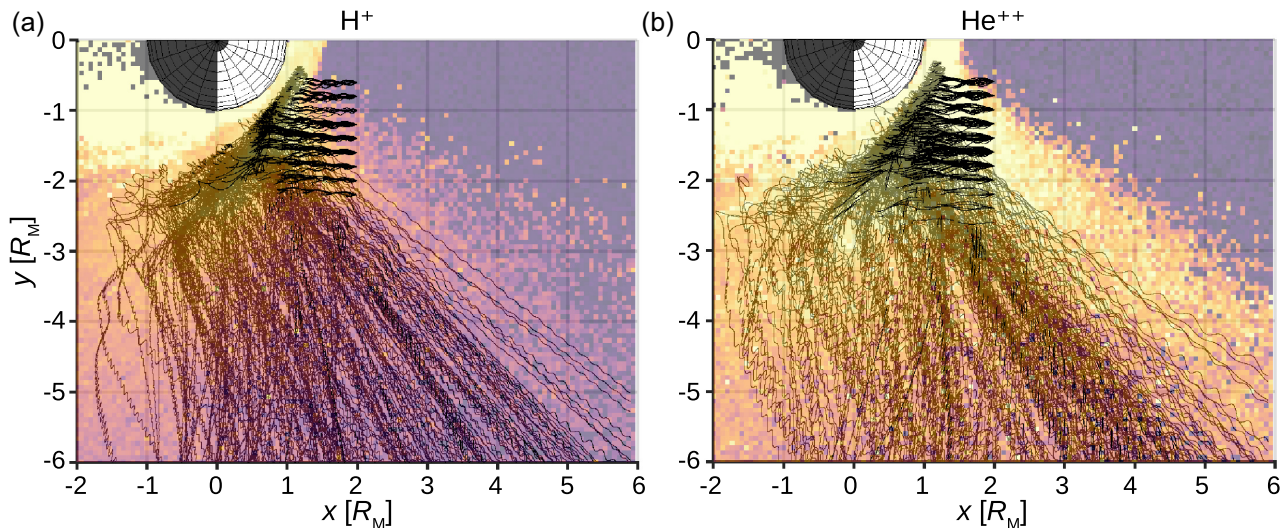


Figure 12. Test particle trajectories of the foreshock (a) protons and (b) alphas. The three-dimensional trajectories are projected on the xy plane as black curves. See text for details of the tracing. Transparent background colouring is the ion temperature at the $z = 0$ plane. (a) The colour scale is the same as in Fig. 2(c) and (d) for protons. (b) The alphas have the same colour scale multiplied by the factor of 3.5.

identical to the Mercury run analysed here except that it contained only the solar wind flow and no planetary environment. We compared this ‘baseline run’ to the point P2 in the quasi-perpendicular side of the bow shock in the analysed Mercury run. The comparison showed similar temporal and spectral features at P2 and the freely flowing solar wind. Thus, the magnetic field and density fluctuations at P2 (at much lower PSDs than at P1) are not caused by the bow shock or the planetary environment in general, but are associated with the undisturbed solar wind flow and its statistical fluctuations in the model. Also, spectral features of the density at frequencies above ~ 1 Hz at P1 (Fig. 4b) are similar to those at P2 and are caused by the statistical fluctuations. There are no backstreaming ions at P2 neither in the empty box nor in the analysed run and there is no considerable spectral power above the gyro frequencies of the solar wind ions in the upstream region on the $z = 0$ plane. This means that the ~ 2 Hz (0.5 s) whistler waves commonly observed upstream of Mercury’s bow shock (Le et al. 2013) do not show up in the model spectra. The processes generating these waves likely involve kinetic electron physics or ion physics below the grid resolution, which are topics that call for future Mercury studies.

There are several topics related to the ion foreshock and the foreshock ULF waves at Mercury, which call for their own detailed studies. We observe a somewhat asymmetric extent of the foreshock between the $z > 0$ and $z < 0$ hemispheres even though the boundary conditions in the hybrid model run are axially symmetric. While the induced magnetospheres of Venus and Mars have magnetic asymmetries in the direction of the upstream convection electric field (Saunders & Russell 1986; Brecht 1990; Zhang et al. 2010; Jarvinen, Kallio & Dyadechkin 2013; Dong et al. 2019), Mercury has a moderate intrinsic magnetic field and a magnetosphere and, thus, the physics of the foreshock north–south asymmetry should be investigated in future works. We include both of the main ion species in the solar wind, protons and alphas, in our simulation study. The number density of the alphas was set as 4 percent of the proton number density in the undisturbed upstream solar wind. Future works should investigate the role of the alpha-to-proton density ratio in the ULF foreshock waves and different

suprathermal foreshock ion distributions. Further, the simulation run analysed here uses an estimated set of nominal upstream conditions at the perihelion of Mercury. However, the plasma conditions near the Sun and the inner Solar system are highly variable, and the dependence of the Hermean foreshock on the magnitude and orientation of the IMF as well as the solar wind density, temperature, and speed should be studied (Winslow et al. 2013; DeForest et al. 2018; Horbury, Matteini & Stansby 2018). Also, the role of any planetary ion populations upstream of the quasi-parallel bow shock on the ULF wave activity should be examined (Raines et al. 2013).

The simulation encourages upcoming BepiColombo operations at Mercury to include an attempt to observe the foreshock ion population ahead of the quasi-parallel Hermean bow shock and the ULF fluctuations in plasma density and magnetic field.

5 CONCLUSIONS

We have studied the solar wind interaction with Mercury using a global three-dimensional hybrid model. The upstream solar wind and IMF conditions correspond to the orbital perihelion of the planet in our simulation case. In the analysis, we find a well-developed, dynamic Hermean ion foreshock ahead of the quasi-parallel region of the Mercury’s bow shock. The ion foreshock contains a portion of the incident solar wind ion flux scattered back upstream near the quasi-parallel bow shock including both the solar wind protons and alphas, which are the major solar wind ion species. These scattered ions form the Hermean suprathermal foreshock ion population. A significant part of the suprathermal population is backstreaming with a velocity component towards the Sun in the near-foreshock at the planetocentric distance of few planetary radii in the plane of the IMF. Finally, the ion foreshock is associated with large-scale, oblique fast magnetosonic waves in the ULF range convecting downstream with the solar wind. In the analysed upstream condition case, the Hermean foreshock ULF wave period is about 5 s, which corresponds to the 30-s foreshock waves at Earth when scaled by the IMF magnitude.

ACKNOWLEDGEMENTS

This work was supported by the Academy of Finland (Decision No. 310444). The authors thank G. Facskó and the ISSI (International Space Science Institute) and ISSI-BJ (International Space Science Institute Beijing) team ‘Dayside Transient Phenomena and Their Impact on the Magnetosphere-Ionosphere’ for discussions and suggestions. Figs 1 and 2 were created using the VisIt open-source visualization tool (Childs et al. 2012). Global three-dimensional hybrid simulations were performed using the RHybrid simulation platform, which is available under an open-source licence by the Finnish Meteorological Institute (<https://github.com/fmihpc/rhybrid/>). The simulation data that support the findings of this study are available from the corresponding author upon reasonable request.

REFERENCES

- Alho M., 2016, Hybrid Plasma Modelling of Lunar Magnetic Anomalies, Master’s thesis, Univ. Helsinki
- Anderson B. J. et al., 2011, *Science*, 333, 1859
- Asbridge J. R., Bame S. J., Strong I. B., 1968, *J. Geophys. Res.*, 73, 5777
- Brecht S. H., 1990, *Geophys. Res. Lett.*, 17, 1243
- Burgess D., Möbius E., Scholer M., 2012, *Space Sci. Rev.*, 173, 5
- Childs H. et al., 2012, High Performance Visualization: Enabling Extreme-Scale Scientific Insight, CRC Press, New York, p. 357
- DeForest C. E., Howard R. A., Velli M., Viall N., Vourlidis A., 2018, *ApJ*, 862, 18
- Dong Y. et al., 2019, *J. Geophys. Res.*, 124, 4295
- Eastwood J. P., Lucek E. A., Mazelle C., Meziane K., Narita Y., Pickett J., Treumann R. A., 2005, *Space Sci. Rev.*, 118, 41
- Edmiston J. P., Kennel C. F., 1984, *J. Plasma Phys.*, 32, 429
- Exner W., Heyner D., Liuzzo L., Motschmann U., Shiota D., Kusano K., Shibayama T., 2018, *Planet. Space Sci.*, 153, 89
- Fairfield D. H., Behannon K. W., 1976, *J. Geophys. Res.*, 81, 3897
- Fatemi S., Poirier N., Holmström M., Lindkvist J., Wieser M., Barabash S., 2018, *A&A*, 614, A132
- Finlay C. C. et al., 2010, *Geophys. J. Int.*, 183, 1216
- Fuselier S. A., 1994, *Solar Wind Sources of Magnetospheric Ultra-Low-Frequency Waves*, *Geophys. Monogr. Ser. 81*, AGU, Washington, D.C., p. 107
- Fuselier S. A., 1995, *Adv. Space Res.*, 15, 43
- Fuselier S. A., Thomsen M. F., Gosling J. T., Bame S. J., Russell C. T., 1986, *J. Geophys. Res.*, 91, 91
- Gary S. P., 1991, *Space Sci. Rev.*, 56, 373
- Gazis P. R., Lazarus A. J., 1982, *Geophys. Res. Lett.*, 9, 431
- Gosling J. T., Thomsen M. F., Bame S. J., Feldman W. C., Paschmann G., Scopke N., 1982, *Geophys. Res. Lett.*, 9, 1333
- Hauck S. A. et al., 2013, *J. Geophys. Res.*, 118, 1204
- Hoppe M. M., Russell C. T., 1982, *Nature*, 295, 41
- Hoppe M. M., Russell C. T., Frank L. A., Eastman T. E., Greenstadt E. W., 1981, *J. Geophys. Res.*, 86, 4471
- Horbury T. S., Matteini L., Stansby D., 2018, *MNRAS*, 478, 1980
- Imber S. M., Slavin J. A., 2017, *J. Geophys. Res.*, 122, 11
- Jarvinen R., Brain D. A., Modolo R., Fedorov A., Holmstrom M., 2018, *J. Geophys. Res.*, 123, 1678
- Jarvinen R., Kallio E., Janhunen P., Pohjola V., Sillanpää I., 2010, in Pogorelov N. V., Audit E., Zank G. P., eds, ASP Conf. Ser. Vol. 429, Numerical Modeling of Space Plasma Flows, Astronom-2009, proceedings of a conference held 29 June through 3 July 2009 in Chamonix. Astron. Soc. Pac., San Francisco, p. 193
- Jarvinen R., Kallio E., Dyadechkin S., 2013, *J. Geophys. Res.*, 118, 4551
- Jarvinen R., Alho M., Kallio E., Wurz P., Barabash S., Futaana Y., 2014, *Geophys. Res. Lett.*, 41, 2243
- Johnson C. L. et al., 2012, *J. Geophys. Res.*, 117, E00L14
- Kallio E., Janhunen P., 2003, *Ann. Geophys.*, 21, 2133
- Kallio E., Janhunen P., 2004, *Adv. Space Res.*, 33, 2176
- Kallio E., Jarvinen R., Janhunen P., 2006, *Planet. Space Sci.*, 54, 1472
- Kennel C. F., 1987, *J. Geophys. Res.*, 92, 13427
- Killen R. et al., 2007, *Space Sci. Rev.*, 132, 433
- Le G., Chi P. J., Blanco-Cano X., Boardsen S., Slavin J. A., Anderson B. J., Korth H., 2013, *J. Geophys. Res.*, 118, 2809
- Ledvina S. A., Ma Y., Kallio E., 2008, *Space Sci. Rev.*, 139, 143
- Marshall W., 1955, *Proc. R Soc. A*, 233, 367
- Omidi N., Blanco-Cano X., Russell C. T., 2005, *J. Geophys. Res.*, 110, A12212
- Omidi N., Blanco-Cano X., Russell C. T., Karimabadi H., 2006, *Adv. Space Res.*, 38, 632
- Orlowski D. S., Crawford G. K., Russell C. T., 1990, *Geophys. Res. Lett.*, 17, 2293
- Orlowski D. S., Russell C. T., Krauss-Varban D., Omidi N., 1995, *Adv. Space Res.*, 16, 143
- Parker E. N., 1958, *ApJ*, 128, 664
- Parks G. K., Lee E., Fu S. Y., Lin N., Liu Y., Yang Z. W., 2017, *Rev. Mod. Plasma Phys.*, 1, 1
- Paschmann G., Scopke N., Papamastorakis I., Asbridge J. R., Bame S. J., Gosling J. T., 1981, *J. Geophys. Res.*, 86, 4355
- Paschmann G., Scopke N., Bame S. J., Gosling J. T., 1982, *Geophys. Res. Lett.*, 9, 881
- Pfleger M. et al., 2015, *Planet. Space Sci.*, 115, 90
- Pohjola V., Kallio E., 2010, *Ann. Geophys.*, 28, 743
- Raines J. M. et al., 2013, *J. Geophys. Res.*, 118, 1604
- Richer E., Chanteur G. M., Modolo R., Dubinin E., 2012, *Geophys. Res. Lett.*, 39, 17101
- Russell C. T., Hoppe M. M., 1983, *Space Sci. Rev.*, 34, 155
- Saunders M. A., Russell C. T., 1986, *J. Geophys. Res.*, 91, 5589
- Shan L., Mazelle C., Meziane K., Delva M., Lu Q., Ge Y. S., Du A., Zhang T., 2016, *J. Geophys. Res.*, 121, 7385
- Shimazu H., 1999, *Earth Planets Space*, 51, 383
- Slavin J. A. et al., 2014, *J. Geophys. Res.*, 119, 8087
- Slavin J. A., Holzer R. E., 1981, *J. Geophys. Res.*, 86, 11401
- Sonnerup B. U. Ö., Scheible M., 1998, Minimum and Maximum Variance Analysis, ISSI Scientific Reports Series 1, ESA Publications Division, Noordwijk, The Netherlands, p. 185
- Trávníček P., Hellinger P., Schriver D., 2007, *Geophys. Res. Lett.*, 34, L05104
- Treumann R. A., 2009, *A&AR*, 17, 409
- Uritsky V. M., Slavin J. A., Khazanov G. V., Donovan E. F., Boardsen S. A., Anderson B. J., Korth H., 2011, *J. Geophys. Res.*, 116, A09236
- Winslow R. M., Anderson B. J., Johnson C. L., Slavin J. A., Korth H., Purucker M. E., Baker D. N., Solomon S. C., 2013, *J. Geophys. Res.*, 118, 2213
- Zhang T. L. et al., 2010, *Geophys. Res. Lett.*, 37, L14202

SUPPORTING INFORMATION

Supplementary data are available at *MNRAS* online.

Please note: Oxford University Press is not responsible for the content or functionality of any supporting materials supplied by the authors. Any queries (other than missing material) should be directed to the corresponding author for the article.

This paper has been typeset from a $\text{\TeX}/\text{\LaTeX}$ file prepared by the author.